RSC Advances

PAPER

View Article Online
View Journal | View Issue

Cite this: *RSC Adv.*, 2025, **15**, 3439

One pot synthesis of SeTe–ZnO nanoparticles for antibacterial and wound healing applications†

Yushu Wang,[a] Shahin Shah Khan,[b] Irfan Ullah,[b] Ahmed Rady,[c] Badr Aldahmash,[c] Yingjie Yu,*[d] Luo Liu*[b] and Xiulong Zhu*[a]

Received 12th September 2024
Accepted 26th January 2025

DOI: 10.1039/d4ra06594h

rsc.li/rsc-advances

Bacterial infections, particularly those involving biofilms, pose significant treatment challenges due to their resistance to traditional antibiotics. Herein, this research explores the integration of selenium–tellurium nanoparticles (SeTe NP) and zinc oxide (ZnO) NP to create hybrid NP with dual photodynamic and photothermal properties. The synthesized SeTe–ZnO NP demonstrated significant efficacy against both Gram-positive *Staphylococcus aureus* (*S. aureus*), *Staphylococcus epidermidis* (*S. epidermidis*) and Gram-negative *Escherichia coli* (*E. coli*), *Pseudomonas aeruginosa* (*P. aeruginosa*) bacteria, effectively disrupting biofilm formation and promoting wound healing. *In vivo* studies further confirmed the biocompatibility and superior wound healing capabilities of SeTe–ZnO NP, highlighting their potential as a versatile and effective treatment for bacterial infections and wound care.

1. Introduction

Bacterial infections pose a significant threat to human health,[1–3] with most of them related to biofilms formed by bacteria and fungi that limit traditional antibiotic treatments, leading to persistent and recurrent infections.[4–8] There have been extensive investigations on the development of biomaterials with dual antibiofilm and antibacterial properties, aiming for synergistic efficacy.[7,9–11] However, achieving this goal involves overcoming hurdles such as complex synthesis and modification processes, which can lead to complex preparation procedures and potential side effects, hindering the practical application of these promising solutions in clinical settings.[12]

In response to microbial infections, research has turned to alternative antimicrobial nanomaterials due to slow progress in developing new antibiotics.[13–16] With the rise of antibiotic resistance, attention has shifted back to metal NP, especially nanometallic materials like gold, silver, platinum, and copper, due to their potent antibacterial properties.[17–20] However, concerns about their toxicity to cells and animals have hindered clinical research.[21] To tackle this, researchers are exploring methods to convert metal nanomaterials into safer metal clusters.[22] Additionally, researchers are also integrating these advanced materials into cutting-edge therapeutic modalities such as photodynamic therapy (PDT) and photothermal therapy (PTT).[23–27] These innovative approaches highlight various applications of nanotechnology in biomedical and antipathogenic technologies, offering promising avenues for revolutionizing treatment strategies against microbial infections.[28–32]

Recently, oxide NP have emerged as antibacterial material due to their cost-effectiveness, nano-scale effects, and unique functionalities.[33] These properties have broadened the use of oxide NP across diverse fields, including antibacterial, antifungal, anti-inflammatory, antimicrobial filters, dental hygiene, medical device disinfection, eye therapies, wound dressings, and catheter coating.[34] Among these NP, ZnO NP stand out for their promising biocompatibility, serving as multifunctional inorganic NP known to enhance the antimicrobial and optical properties.[35,36] This versatility not only augments material performance but also holds promise for the development of safer and more efficient products for biomedical application.

Furthermore, the one-pot synthesis process has been prominent for the synthesis of SeTe NP owing to its simplicity, efficiency, and scalability. This process, executed under hydrothermal or solvothermal conditions, employs increased temperatures and pressures to promote reduction and nucleation, resulting in SeTe NP with excellent stability, reactivity, and tuneable morphologies, which are crucial for biological applications.[37–40] SeTe NP serve as potent antibacterial agents by generating reactive oxygen species (ROS) that compromise microbial cells through oxidative stress, leading to membrane damage, protein denaturation, and intracellular malfunction,

[a]*The People's Hospital of Gaozhou, National Drug Clinical Trial Institution, Gaozhou City 525200, China. E-mail: xl123z@aliyun.com*

[b]*College of Life Science and Technology, Beijing University of Chemical Technology, No. 15 East Road of North Third Ring Road, Beijing 100029, China. E-mail: Liuluo@mail.buct.edu.cn*

[c]*Department of Zoology, College of Science, King Saud University, P.O. Box 2455, Riyadh 11451, Saudi Arabia*

[d]*State Key Laboratory of Organic–Inorganic Composites, Beijing University of Chemical Technology, Beijing 100029, China. E-mail: yuyingjie@mail.buct.edu.cn*

† Electronic supplementary information (ESI) available. See DOI: https://doi.org/10.1039/d4ra06594h

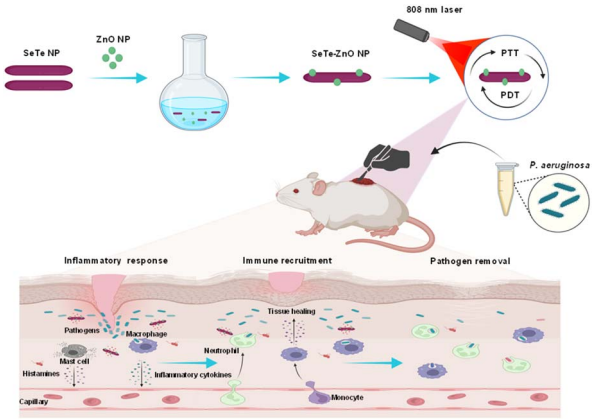

Fig. 1 Schematic illustration showing SeTe–ZnO NP synthesis and their antibacterial and wound healing mechanism.

thereby demonstrating efficacy against antibiotic-resistant infections.[41] Prior research has underscored their exceptional antibacterial effectiveness relative to single selenium or tellurium NP, demonstrating significant activity against pathogens including *E. coli* and *S. aureus*.[42–44] These findings underscore the potential of SeTe NP as a scalable and robust solution to combat antimicrobial resistance, paving the way for diverse biomedical and environmental applications.

Herein, this study reports a one-pot synthesis technique for SeTe–ZnO NP, designed for dual-mode therapeutic properties. As illustrated in Fig. 1, by integrating photothermal and photodynamic properties, these NP exhibit significant capabilities against bacterial infections, substantially amplifying their antibacterial efficacy. Notably, the significant proficiency of SeTe–ZnO NP in eradicating both Gram-positive *S. aureus* and *S. epidermidis*, as well as Gram-negative *E. coli* and *P. aeruginosa*, effectively targeting biofilm forming pathogens. Furthermore, beyond their impressive antibacterial and anti-biofilm capabilities, SeTe–ZnO NP exhibit promising wound healing properties. Overall, this study demonstrates the versatility of SeTe–ZnO NP as an excellent platform for eradicating bacterial infections.

2. Experimental

2.1. Materials, bacterial strains and animals

The chemicals used in the current study were obtained from Sigma Aldrich, St. Louis, MO, USA, including sodium selenite (Na_2SeO_3), telluric acid (H_6TeO_6), ZnO NP (<50 nm particle size), cetyltrimethylammonium bromide (CTAB), ascorbic acid, hydrazine, 2,2,6,6-tetramethylpiperidine (TEMP), 4,6-diamidino-2-phenylindole (DAPI), 5,5-dimethyl-1-pyrroline-*N*-oxide (DMPO), and 2,7-dichlorofluorescein diacetate (DCFH-DA). The bacterial strains, *E. coli* (ATCC8739), *P. aeruginosa* (ATCC10145), *S. aureus* (ATCC6538), and *S. epidermidis* (ATCC14990), were obtained from Chinese Academy of Sciences, Beijing, China. BALB/c mice (18–20 g, 6–7 weeks) were used and supplied by SPF (Beijing) Biotechnology Co. Ltd, China.

2.2. Synthesis of SeTe–ZnO NP

For synthesis of SeTe–ZnO NP, SeTe NP were first prepared following a previously published method.[37,38] Briefly, telluric acid (20 mM) and sodium selenite (20 mM) solutions were prepared separately in the presence of 2 mg per mL CTAB, with the final volume adjusted to 100 mL using dH_2O. Following a 30 min sonication, the solution was stirred in an oil bath at 95 °C for 3 h. Subsequently, a combination of reducing agents, hydrazine (500 μL) and ascorbic acid (100 mg mL^{-1}), dissolved in 10 mL of dH_2O, was dropwise introduced into the reaction mixture and maintained at 95 °C for an additional 30 min. This step led to a notable color change from colorless to a deep grey. Finally, the product was subjected to collection and purification through centrifugation at 15 000 rpm for 10 min with 50% ethanol for three times, followed by drying at 60 °C overnight.

Subsequently, SeTe–ZnO NP were prepared using SeTe NP following the above-mentioned method. SeTe NP (300 mg) were dissolved in 30 mL of water and subjected to 30 min sonication. Simultaneously, ZnO NP (20 mM) were also dissolved in 10 mL of water through sonication for an equivalent duration. The two solutions were subsequently combined dropwise, with rigorous stirring maintained at 75 °C for 2 h. To minimize the presence of residual materials, 3 mL of hydrazine was introduced into the solution. Finally, the SeTe–ZnO NP were isolated and purified using centrifugation for 10 min at 15 000 rpm using 50% ethanol for three times, followed by overnight drying at 60 °C.

2.3. Antibacterial and antibiofilm analysis

The antibacterial activity of SeTe–ZnO NP were analyzed using agar well diffusion against *S. aureus*, *S. epidermidis*, *E. coli*, and *P. aeruginosa*.[45] Zones of inhibitions were measured following a 24 h incubation time to assess the antibacterial activity of NP. Moreover, antibacterial activity was also evaluated against the test bacterial strains using agar plate method. Various concentrations of SeTe–ZnO NP *i.e.*, 5, 10, 20, and 40 μg mL^{-1} were added to bacterial solutions and the solutions were irradiated with 808 nm laser for five min at a power density of 1 W cm^{-2}. Followed by 2 h incubation at 37 °C. Subsequently, 100 μL of bacteria was spread on plate and incubated overnight.

Furthermore, to investigate the antibiofilm efficacy of SeTe–ZnO NP, a bacterial cell culture with an initial optical density (OD) of 0.025 at 600 nm was inoculated into a 96-well plate and incubated at 37 °C for 24 h. After the formation of biofilm on the wells, the media was removed by inverting the plate, and any planktonic cells were eliminated by washing the biofilm with phosphate-buffered saline (PBS). Subsequently, varying concentrations of SeTe–ZnO NP (5, 10, 20, and 40 μg mL^{-1}) were added to the wells, with the PBS-treated group as the negative control. Following incubation, the biofilm was fixed by the addition of 0.5% crystal violet solution with methanol for 15 min. After rinsing the biofilm with sterile PBS, the crystal violet was dissolved using acetic acid (33% v/v) with gentle

shaking for 10 min. Biofilm quantification was achieved by measuring the absorbance at 590 nm using a 96-well microplate reader.

2.4. Bacterial live/dead assay

To evaluate the viability of bacteria, a fluorescence-based live/dead assay method was employed.[46] Overnight cultured bacteria (1.5 mL) were collected and washed with PBS, followed by treatment with SeTe–ZnO NP and irradiated with 808 nm laser for five min with a power density of 1 W cm^{-2}. Following this, the mixture was allowed to culture for 1 h. Subsequently, DAPI (50 μL) and PI (50 μL), fluorescent dye were introduced into the solution, with a concentration of 30 μM. The mixture was then left to incubate for an additional 15 min. To eliminate any excess dye, the samples were washed three times with PBS. For the observation of the samples, a confocal laser scanning microscopy (CLSM) system (Leica DMI 4000 B, Germany) was employed to capture high-resolution images.

2.5. Intracellular ROS detection

To evaluate intracellular ROS generation by SeTe–ZnO NP, DCFH-DA probe was used.[47–49] In a 20 mL solution of 0.9% NaCl, intracellular ROS dye DCFH-DA (10 μM) was added and co-incubated for 30 min with bacterial cells at a concentration of 1×10^6 CFU mL^{-1}. Subsequently centrifugation at 8000 rpm for 5 min was used to separate the DCFH-DA from the bacterial cells. The bacterial cells were treated as follows: PBS, PBS with 808 nm laser irradiation (PBS + L), SeTe–ZnO NP, and SeTe–ZnO NP with 808 nm laser irradiation (SeTe–ZnO NP + L). 808 nm laser irradiation was performed for 5 min, followed by a 4 h incubation at 37 °C. Fluorescence intensity was measured using a fluorometer, while observation and photos were taken using a CLSM.

2.6. SEM assessment of bacteria

The bacterial cells cultured overnight, were harvested and subjected to washing three times, followed by treatment with 20 μg mL^{-1} of both SeTe NP and SeTe–ZnO NP for 1 h for scanning electron microscope (SEM) analysis. Following irradiation with 808 nm laser for 10 min, all samples were centrifuged at 5000 rpm and subsequently washed with PBS. Next, the cells were fixed overnight with a 2.5% glutaraldehyde solution at 4 °C, followed by dehydration using various concentrations of ethanol. Finally, the prepared samples were visualized using a scanning electron microscope (SEM, Hitachi SU, 8080, Japan).

2.7. Biocompatibility assessment

Hemolysis test was performed for evaluation of biological toxicity of SeTe–ZnO NP. Fresh mice blood was collected and subjected to centrifugation at 1500 rpm for 15 min to isolate red blood cells, which were then washed thrice with normal saline. The concentrated red blood cells were diluted to 5% and treated with PBS, water, and various concentrations (10, 25, and 50 μg mL^{-1}) of both SeTe NP and SeTe–ZnO NP, incubated at 37 °C for 3 h, followed by centrifugation at 11 000 rpm for 5 min. The supernatant was collected, and absorbance was measured at 540 nm. The hemolysis rate induced by SeTe–ZnO NP was calculated in comparison to the PBS and water-treated groups.

2.8. *In vivo* wound healing performance

All animal experiments reported in this study were conducted in accordance with the guidelines (ZYZY202209005S) assessed and approved by the institutional animal care and use committee of Sino Research (Beijing) Biotechnology Co., Ltd (China).

In vivo wound healing experiments were performed using female BALB/c mice weighing 20 g and aged 6–7 weeks. Skin wounds were created on the dorsal area of each mouse using a previously published method.[50,51] To ensure aseptic conditions, dorsal hairs were removed with 7% sodium sulfide and the area was disinfected using 75% ethanol. A circular wound with an 8 mm diameter was then created using a hole puncher and infected with 10 μL of bacteria at a 10^{-6} dilution factor. After 24 h, 20 μL (20 μg mL^{-1}) of the SeTe–ZnO NP were applied to the wounds of the respective groups, with subsequent applications every second day. Wound images were captured using a camera, and healing wound area was quantified using ImageJ software. The healing wound rate (%) was calculated using the formula:

$$\text{Healing wound rate}(\%) = \frac{\text{area day 0} - \text{area day } X}{\text{area day 0}} \times 100$$

where, area day 0 and area day X represent the wound areas on day 0 and day X, respectively. Histological analysis was performed on days 6 and 12 by collecting wound tissues, fixing them in 10% formalin. The tissues were stained with Harris' hematoxylin solution for 6 h at a temperature of 60–70 °C and were then rinsed in tap water until the water was colorless. The samples were obtained and processed for further analysis.

2.9. Statistical analysis

All data in this study were presented as mean ± SD ($n \geq 3$). GraphPad Prism 8 was used for statistical analysis. Unpaired Student's t-test was used to analyze significant differences between two groups, while ANOVA with Tukey's multiple comparison test was employed for analysis among multiple groups. The threshold for statistical significance was set at $p < 0.05$.

3. Results and discussion

3.1. Preparation and characterization of SeTe–ZnO NP

3.1.1. Morphological assessment. The surface morphology of the synthesized SeTe–ZnO NP prepared using one-pot method, was examined using transmission electron microscope (TEM). In Fig. 2a, the TEM images shows that SeTe NP have rod-shaped morphology while ZnO NP exhibit irregular morphology. SeTe–ZnO NP were found homogeneously distributed. Notably, SeTe–ZnO NP exhibit a unique morphology with features from both SeTe NP and ZnO NP, indicating effective hybridization. These SeTe–ZnO NP show an interconnected network structure, which could potentially

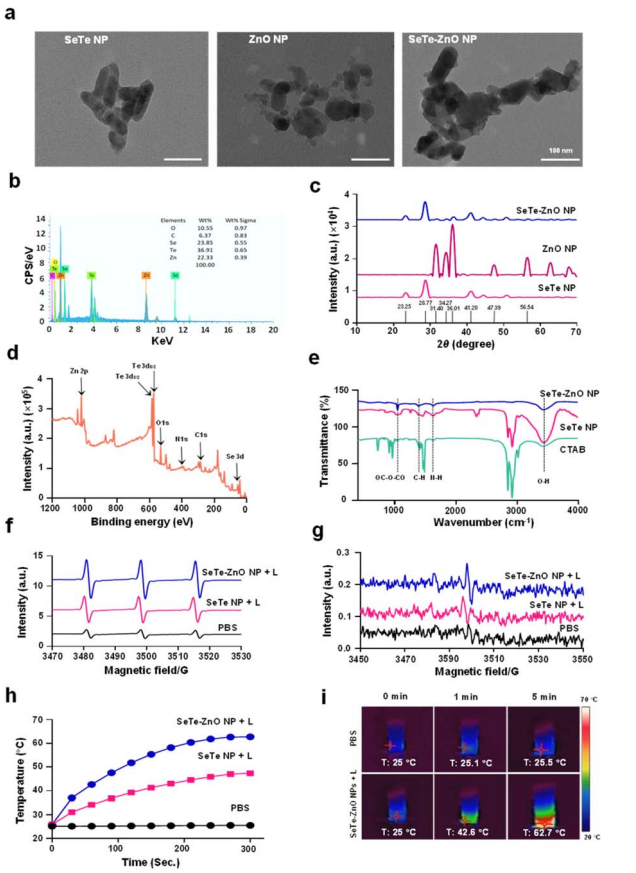

Fig. 2 Characterization of SeTe–ZnO NP. (a) TEM images of SeTe NP, ZnO NP, and SeTe–ZnO NP. (b) EDS spectrum of SeTe–ZnO NP. (c) XRD spectra of SeTe NP, ZnO NP, and SeTe–ZnO NP. (d) XPS survey spectra of SeTe–ZnO NP. (e) FTIR spectra of CTAB, SeTe NP, and SeTe–ZnO NP. (f) EPR spectra of singlet oxygen generation of PBS, SeTe NP + L, and SeTe–ZnO NP + L. (g) EPR spectra of hydroxyl radical generation of PBS, SeTe NP + L, and SeTe–ZnO NP + L. (h) Heat generation of PBS, SeTe NP and SeTe–ZnO NP under 808 nm laser irradiation for 5 min. (i) Thermal images of heat generation by PBS and SeTe–ZnO NP under 808 nm laser irradiation for 5 min.

enhance their functional properties. Furthermore, the elemental composition of the NP was analyzed using energy-dispersive X-ray spectroscopy (EDS). The basic spectral outline obtained from EDS confirmed the presence of metalloids, as high-resolution mapping and spectra displayed Se, Te, Zn, and O (Fig. 2b and S1†). These findings show the successful synthesis of SeTe–ZnO NP, highlighting the effective amalgamation of these elements within the nanostructures.

3.1.2. X-ray crystallography. The crystalline structure of the SeTe–ZnO NP was examined using an X-ray diffractometer at 25 °C. Intensity data was obtained within a 2θ range from 5° to 90° (Fig. 2c). The prominent diffraction peaks appeared at $2\theta =$ 28.77° and 40.10° shows SeTe NP in the (101) lattice plane.[38] Furthermore, ZnO NP were incorporated on the surface of SeTe NP. The typical crystal structures diffraction peaks of SeTe–ZnO NP are reflected at 28.77°, 36.5°, 40.1°, 44.30°, and 50.74° as compared to ZnO NP. The sharpness and intensity of these peaks suggest a high degree of crystallinity and phase purity. The diffraction pattern confirms the successful synthesis of SeTe–ZnO NP.

3.1.3. X-ray photoelectron spectroscopy (XPS). The binding energies of SeTe NP and SeTe–ZnO NP were investigated using XPS. The XPS spectrum confirmed the presence of individual elements Se, Te, O, and Zn within the composite NP, as depicted in Fig. 2d. The binding energies for each component in SeTe–ZnO NP were analyzed, with detailed spectra presented in Fig. S2,† confirming the incorporation of ZnO NP on the surface of the bimetallic SeTe NP. Two significant peaks for Zn 2p were deconvoluted, revealing binding energies of 1020.6 eV and 1043.5 eV. The deconvoluted Te 3d spectrum exhibited four distinct bands at binding energies of 573.5, 575.9, 583.9, and 586.5 eV. The peaks at 583.9 eV and 573.5 eV correspond to Te(0) $3d_{3/2}$ and $3d_{5/2}$, respectively, while the other two bands indicate the presence of Te(IV) 3d, suggesting that Te exists in both elemental and oxide forms. Additionally, the Se 3d spectrum reveals bands at 55.1 eV (Se $3d_{5/2}$) along with a broad band around 58.6 eV, attributed to the SeO_2 bond in SeTe–ZnO NP. These findings collectively confirm the successful synthesis and surface composition of SeTe–ZnO NP.

3.1.4. Fourier transform infrared (FTIR) spectroscopy. The FTIR spectrum of SeTe–ZnO NP acquired in the range of 100–4000 cm^{-1} is presented in Fig. 2e. The strong, broad peak observed at 3438 cm^{-1} could be attributed to the stretching vibrations of O–H groups. Peak around 1628 cm^{-1} correspond to the N–H bending vibrations associated with amide groups. The bands at 1388 cm^{-1} are indicative of C–H bending vibrations. Additionally, the CO–O–CO stretching vibrations are reflected in the band at 1046 cm^{-1}.

3.2. Photodynamic and photothermal assessment

3.2.1. Photodynamic assessment. EPR analysis was employed to investigate the generation of ROS. 808 nm laser (1 W cm^{-2}, 1–5 min) was applied to both SeTe NP and SeTe–ZnO NP. TEMP and DMPO were used to detect the release of singlet oxygen and hydroxyl radicals, respectively. TEMP, a common trapping agent for singlet oxygen, was utilized for both SeTe NP and SeTe–ZnO NP, resulting in the formation of the TEMPO adduct upon reaction with $^1O_2$. The EPR spectra for singlet oxygen generation for SeTe NP and SeTe–ZnO NP upon irradiation with 808 nm laser are depicted in Fig. 2f. The EPR spectra becomes more prominent with the doping of ZnO NP on the surface of SeTe NP and with the application of 808 nm laser irradiation. This enhancement suggests that the ZnO NP significantly boosts the generation of singlet oxygen. The increased signal intensity can be attributed to the photocatalytic properties of ZnO NP, which likely facilitates more efficient generation of $^1O_2$. Fig. S3b† represents singlet oxygen generation spectra for SeTe NP and SeTe–ZnO NP without irradiation with 808 nm laser. Additionally, DMPO, a hydroxyl radical trapping agent, was used to analyze the same samples. Upon irradiation with the 808 nm laser for 1–5 min, prominent signals indicative of hydroxyl radicals was recorded by EPR as shown in Fig. 2g, while hydroxyl radical spectra without 808 nm laser irradiation is depicted in Fig. S3a.† The effective

generation of singlet oxygen and hydroxyl radicals by SeTe NP and SeTe–ZnO NP under 808 nm laser irradiation can be attributed to surface-capped proteins and exposed oxygen vacancies. The excitation of electrons in the samples by the 808 laser is likely to facilitate ROS production. This enhancement underscores the potential of SeTe–ZnO NP for applications requiring effective ROS generation.

3.2.2. Photothermal assessment. The synthesized SeTe NP and SeTe–ZnO NP were evaluated for its photothermal performance upon 808 nm laser irradiation (1 W cm^{-2}). The temperature of the solution increased in a concentration-dependent manner, with the solution containing 50 μg mL^{-1} NP reaching up to 62.7 °C within 5 min. In comparison, the temperature of SeTe NP reached 47.37 °C, while the PBS control was recorded at 25.5 °C (Fig. 2h). The corresponding photothermal images are depicted in Fig. 2i. In addition, to assess the photothermal stability of SeTe–ZnO NP, the samples were subjected to 808 nm laser irradiation for 5 min, followed by natural cooling to room temperature for another 5 min, in a cycle repeated five times (Fig. S4b†). The photothermal effect of the SeTe–ZnO NP solution showed minimal change and only slight degradation over the five on/off cycles, demonstrating excellent photothermal stability of the NP. Additionally, a single heating/cooling cycle of SeTe–ZnO NP under 808 nm laser irradiation is shown in Fig. S4a.† These findings suggest that the photothermal properties of SeTe NP can be significantly enhanced by the incorporation of ZnO NP, indicating their potential for applications requiring stable and efficient photothermal performance.

3.3. Antibacterial and antibiofilm activity

3.3.1. Zones of inhibition. The bactericidal activity of SeTe–ZnO NP was assessed using the zone of inhibition assay, which directly correlates with bactericidal effectiveness. The results showed that SeTe–ZnO NP exhibited exceptionally high bactericidal activity against both *E. coli* and *P. aeruginosa*, with inhibition zones measuring 27 ± 1 mm and 29 ± 1 mm, respectively, while inhibition zones recorded against *S. aureus* and *S. epidermidis* were each 9 ± 1 mm (Fig. 3a and S5†). It revealed that SeTe–ZnO NP had significantly enhanced bactericidal activity against both Gram-negative and Gram-positive bacteria. These findings underscore the superior antimicrobial properties of SeTe–ZnO NP.

3.3.2. Antibiofilm assessment. Biofilm formation on 96-well microtiter plates was analyzed for various bacterial strains using the crystal violet method, which stains both cellular and matrix components of biofilms. SeTe–ZnO NP significantly reduced mature biofilm mass across all strains, particularly in *P. aeruginosa* and *E. coli* (Fig. 3b). SeTe–ZnO NP treatment reduced *E. coli* and *P. aeruginosa* biofilm mass to less than 20%, while SeTe–ZnO NP treatment reduced *S. aureus* and *S. epidermidis* biofilm mass to about 50% and 60%, respectively. These results indicate that SeTe–ZnO NP effectively inhibit biofilm formation, suggesting potential biomedical applications.

3.3.3. Agar plate method for antibacterial assessment. The agar plate method was utilized to examine the impact of NP on bacterial growth, both in the presence and absence of 808 nm laser irradiation (Fig. 3c and S6†). The results indicated that SeTe–ZnO NP exhibited significant antibacterial activity against all the tested bacterial strains. The antibacterial efficacy of SeTe–ZnO NP was enhanced when combined with 808 nm laser irradiation, demonstrating superior bactericidal properties. This synergy between SeTe–ZnO NP and 808 nm laser irradiation led to a significant increase in bacterial inhibition, highlighting the potential of this approach for advanced antibacterial treatments. These findings suggest that SeTe–ZnO NP, especially when activated by 808 nm laser, could serve as powerful antibacterial agents for combating bacterial infections.

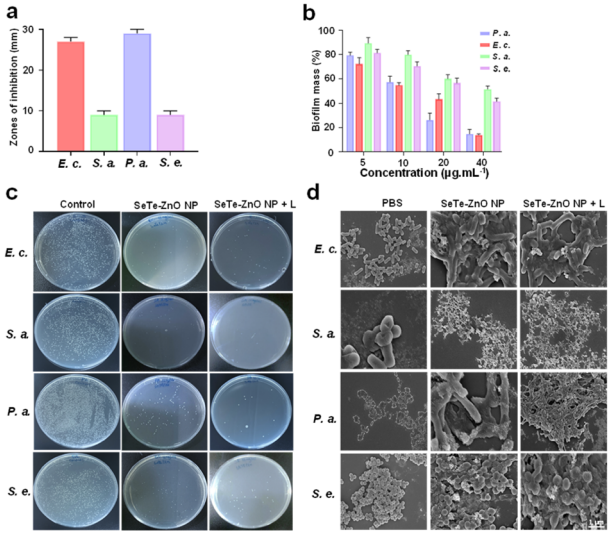

Fig. 3 *In vitro* antibacterial activity of SeTe–ZnO NP. (a) Zones of inhibitions of SeTe–ZnO NP against *E. coli*, *S. aureus*, *P. aeruginosa*, and *S. epidermidis*. (b) Antibiofilm activity of different concentrations of SeTe–ZnO NP against *E. coli*, *S. aureus*, *P. aeruginosa*, and *S. epidermidis*. (c) Antibacterial activity of SeTe–ZnO NP and SeTe–ZnO NP + L using agar plate method. (d) SEM images of bacteria after treatment with PBS, SeTe–ZnO NP, and SeTe–ZnO NP + L.

3.3.4. Bacterial membrane damage study. To further confirm the antibacterial activity of the synthesized NP, bacterial cultures treated with various NP were analyzed for membrane disruption. SEM images of untreated *S. aureus* and *S. epidermidis* cells revealed their typical spherical shape with intact, smooth surfaces, while *E. coli* and *P. aeruginosa* cells exhibited their characteristic rod shape. However, exposure to the NP resulted in significant changes to the bacterial cell surfaces. The synthesized SeTe–ZnO NP, in particular, caused significant membrane damage, as evidenced by SEM images (Fig. 3d). The membrane damage increased the permeability which facilitated the entry of SeTe–ZnO NP into the bacterial cells, thereby enhancing their bactericidal efficiency. These observations indicate that SeTe–ZnO NP are highly effective in disrupting bacterial membranes.

3.3.5. Live/dead assay. To confirm the membrane-disruptive effects of SeTe–ZnO NP, CLSM was employed using

bacterial cells stained with DAPI and PI. DAPI stains all cells by binding to DNA, emitting blue fluorescence, while PI only penetrates cells with compromised membranes, indicating cell death through red fluorescence. In Fig. 4a, CLSM images show that bacteria treated with SeTe–ZnO NP exhibited red fluorescence showing dead bacteria, while untreated cells exhibited blue fluorescence, indicating intact membranes that prevent PI entry. While bacteria treated with SeTe–ZnO NP + L the ratio of live/dead bacteria was higher, suggesting membrane integrity impairment. These results demonstrate the potent membrane-disruptive activity of SeTe–ZnO NP, validating their effectiveness in compromising bacterial cell membrane integrity and inducing cell death.

3.4. Antibacterial mechanism

The antibacterial mechanism of SeTe–ZnO NP involves several interconnected pathways that collectively contribute to their potent antimicrobial properties. One primary mechanism is the interaction of SeTe–ZnO NP with bacterial cell membranes. Due to their small size and positive surface charge, ZnO NP can adhere to the negatively charged bacterial membrane, causing structural damage, increasing membrane permeability, and leading to leakage of cellular contents, which ultimately results in cell lysis and death.[52] Therefore, SEM and CLSM of the SeTe–ZnO NP and SeTe–ZnO NP + L treated bacteria were analyzed as shown in Fig. 3d and 4a, respectively, which confirms the cell membrane disruption of the bacterial cells.

Another critical mechanism is the generation of ROS by SeTe–ZnO NP. When ZnO NP interact with the bacterial cell, they can produce ROS such as hydrogen peroxide, superoxide anions, and hydroxyl radicals. These ROS induce oxidative stress within the bacterial cells, damaging vital cellular components such as DNA, proteins, and lipids. This oxidative damage disrupts normal cellular functions and can trigger apoptosis pathways, leading to cell death. The change in ROS levels due to SeTe–ZnO NP, and SeTe–ZnO NP + L was assessed as illustrated in Fig. 4b. The associated fluorescence intensities reveal an increase in green fluorescence following the sequence: PBS, SeTe–ZnO NP, and SeTe–ZnO NP + L (Fig. S7†). This pattern indicates an increase in ROS production. Moreover, these findings confirm the production of hydroxyl radicals by SeTe–ZnO NP + L. This induced oxidative stress within the cell is likely responsible for initiating bacterial apoptosis. Elevated ROS levels can greatly disrupt the function and integrity of bacterial biomacromolecules, underscoring the bactericidal efficacy of SeTe–ZnO NP. These observations clearly demonstrate that the enhanced bactericidal effect of SeTe–ZnO NP is due to the increased production of ROS. Additionally, the dissolution of ZnO NP leads to the release of zinc ions (Zn^{2+}), which further enhance their antibacterial activity. These ions can interfere with various metabolic pathways and enzyme functions within the bacterial cell. The disruption of zinc ion homeostasis contributes to further oxidative stress and cellular damage, complementing the effects of ROS and direct interaction of NP.

Overall, the above results demonstrated that the antibacterial action of SeTe–ZnO NP is a result of the combined effects of membrane disruption, ROS generation and zinc ion release. These mechanisms work synergistically to cause substantial damage to bacterial cells, making SeTe–ZnO NP effective against a broad spectrum of bacterial pathogens, including drug resistant strains. The versatility and efficacy of SeTe–ZnO NP underscore their potential as powerful antibacterial agents in various applications.

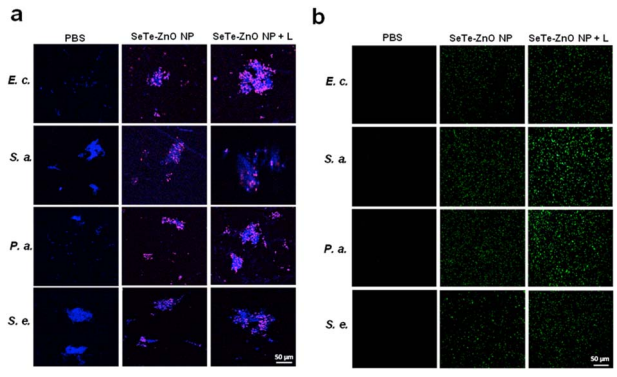

Fig. 4 *In vitro* antibacterial activity and intracellular ROS generation by SeTe–ZnO NP. (a) CLSM images of live/dead bacteria treated with PBS, SeTe–ZnO NP and SeTe–ZnO NP + L. (b) CLSM images showing intracellular ROS generation of bacteria after treatment with PBS, SeTe–ZnO NP and SeTe–ZnO + L.

3.5. Biocompatibility assessment

It is crucial to assess the biosafety of SeTe–ZnO NP before it can be used for *in vivo* application. A hemolysis assay was conducted to evaluate the effect of SeTe–ZnO NP on the hemolysis of red blood cells, with pure water and PBS treated samples taken as positive and negative controls, respectively. The results demonstrated that the hemolysis ratios were below 5% across all tested concentrations (Fig. S8†), indicating the promising blood compatibility of SeTe–ZnO NP. These findings indicate that the synthesized NP exhibit minimal hemolytic activity, making them a promising candidate for *in vivo* studies.

3.6. Infected wound healing activity

Bacterial infections in wounds can affect healing by producing toxins and triggering inflammatory responses.[53,54] Given the demonstrated antibacterial properties of SeTe–ZnO NP, their efficacy in promoting wound healing was evaluated using a mouse skin wound model infected with *P. aeruginosa*. The wounds were treated with SeTe–ZnO NP, SeTe–ZnO NP + L and PBS. Macroscopic views of wound healing at various intervals and its corresponding healing area are shown in Fig. 5b, while Fig. 5a provides a schematic representation of the treatment process for each group. Wounds treated with SeTe–ZnO NP and SeTe–ZnO NP + L showed accelerated healing, with scabs falling off and new tissue regenerated. Compared to the PBS treatment group, the SeTe–ZnO NP + L group exhibited significantly faster wound closure, with smaller wound areas observed over time. After 10 days, the healing rates were 85.45% for SeTe–ZnO NP and, 95.04% for SeTe–ZnO NP + L (Fig. 5c and S9†). The PBS

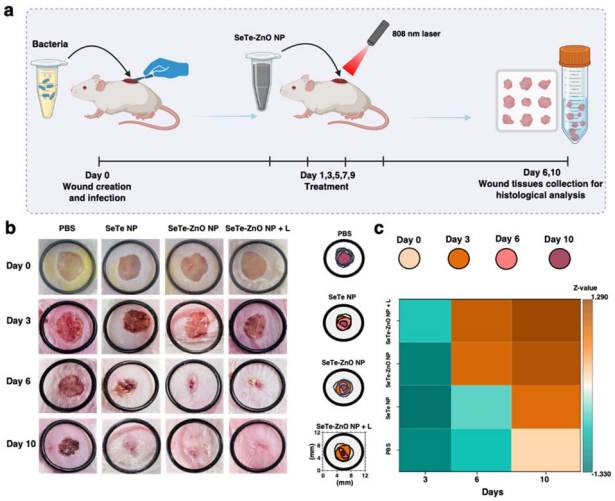

Fig. 5 Infected wound healing assessment of SeTe–ZnO NP. (a) Schematic illustration of the treatment process for *in vivo* study. (b) Healing wound images and corresponding healing wound area at different days after treatment with PBS, SeTe NP, SeTe–ZnO NP, and SeTe–ZnO NP + L. (c) Heat map displaying wound healing activity for each treatment group at different days, deep orange color represents the highest wound healing.

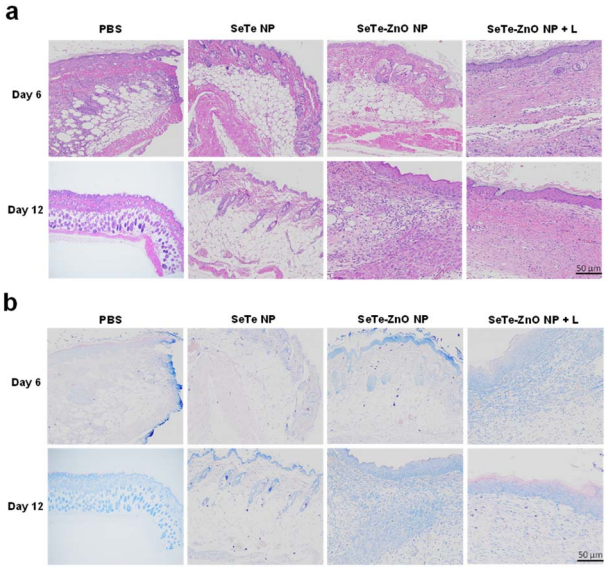

Fig. 6 Histological assessment of the wound tissues. (a) H&E staining of the wound tissues of different treatment groups (PBS, SeTe NP, SeTe–ZnO NP and SeTe–ZnO NP + L) at days 6 and 12. (b) Giemsa staining of the wound tissues after treatment with PBS, SeTe NP, SeTe–ZnO NP, and SeTe–ZnO NP + L at day 6 and day 12.

treatment group exhibited the slowest healing, with persistent scabbing. Additionally, the treated mice did not experience any weight loss (Fig. S10†), indicating that SeTe–ZnO NP are safe for *in vivo* application. These results demonstrate the superior efficacy of SeTe–ZnO NP in killing bacteria at the wound site, thereby mitigating bacterial damage and enhancing wound healing. The improved healing rate with SeTe–ZnO NP is also attributed to their photodynamic and photothermal activity, which helps eliminate bacteria.

3.7. Hematoxylin and eosin staining

Histological analysis using hematoxylin and eosin (H&E)[55,56] staining was conducted to assess the impact of SeTe–ZnO NP on wound healing (Fig. 6a). At 6 days post-wounding, laser-induced wounds treated with SeTe–ZnO NP exhibited rapid re-epithelialization as compared to those treated with the PBS. Granulation tissue formation was evident in the SeTe–ZnO NP treated group accompanied by increased infiltration of inflammatory cells. Additionally, the number of inflammatory cells were higher in the SeTe–ZnO NP + L treated group than in the PBS treated group. After 12 days of treatment, the wounds in the SeTe–ZnO NP treated group were fully re-epithelialized. In contrast, the PBS treated group exhibited a thin layer with more inflammatory cells in the loose connective tissue over the wound surface.

3.8. Giemsa staining of the wound tissues

Giemsa staining was performed for the collected tissues on days 6 and 12 to assess any bacterial residues. As shown in Fig. 6b, a significant bacterial load was observed in the PBS, SeTe–ZnO NP, and SeTe–ZnO NP + L treatment groups on day 6. By day 12, the SeTe–ZnO NP and SeTe–ZnO NP + L groups exhibited a noticeable reduction in bacterial residues compared to the PBS group, showing fewer bacterial residues. Particularly, the SeTe–ZnO NP + L treatment group showed no detectable signs of infection or bacteria. These findings indicate that SeTe–ZnO NP possess potent antibacterial activity, significantly enhanced by 808 nm laser irradiation, thus supporting the *in vitro* antibacterial efficacy. This study underscores the potential of SeTe–ZnO NP, particularly when used with 808 nm laser, as a powerful antibacterial agent for therapeutic applications.

3.9. Quantification of bacteria in wounds

The wound tissues were excised to quantify the presence of bacteria, thereby evaluating the bactericidal efficiency of the synthesized NP. Results from the standard agar plate dilution assay revealed that SeTe–ZnO NP + L exhibited the highest bactericidal activity, as evidenced by the significantly reduced number of bacterial colonies compared to the other treatment groups (Fig. S11†). These results highlight the superior antibacterial efficacy of SeTe–ZnO NP when used with 808 nm laser irradiation.

4. Conclusions

This study successfully demonstrates the one-pot synthesis of SeTe–ZnO NP, which exhibit dual antibacterial and antibiofilm activities, along with enhanced wound healing efficacy. The SeTe–ZnO NP displayed significant antibacterial properties against both Gram-positive and Gram-negative bacteria. This efficacy is attributed to multiple mechanisms of action, such as the disruption of bacterial cell membranes, generation of ROS, and photothermal properties. The ROS generation and

subsequent oxidative stress lead to severe damage to bacterial cellular components, while zinc ions further disrupt bacterial metabolic pathways. *In vivo* studies further validated the biocompatibility and effectiveness of SeTe–ZnO NP in promoting wound healing. The synthesized NP facilitated rapid wound closure, reduced bacterial load, and minimized infection in a mouse model, demonstrating their potential as a safe and effective treatment for bacterial infections and wound management. The combination of photodynamic and photothermal properties significantly enhanced the antibacterial activity, especially when activated by 808 nm laser irradiation. Overall, SeTe–ZnO NP represent a versatile platform for combating bacterial infections and promoting wound healing, highlighting their potential for broad clinical applications. The findings underscore the importance of integrating nanotechnology in developing advanced therapeutic agents to address the challenges posed by antibiotic-resistant bacteria and biofilm-associated infections. Further research and development could optimize these NP for practical clinical use, ensuring their safety and efficacy in diverse biomedical applications.

Data availability

The data supporting this article have been included as part of the ESI.†

Author contributions

Yushu Wang: experimental work, writing original draft. Shahin Shah Khan: conceptualization, experimental work, data analysis. Irfan Ullah: data analysis. Ahmed Rady: conceptualization. Badr Aldahmash: conceptualization. Yingjie Yu: supervision and reviewing the draft. Luo Liu: conceptualization, supervision, draft modification. Xiulong Zhu: supervision.

Conflicts of interest

There are no conflicts to declare.

Acknowledgements

The authors gratefully acknowledge the financial support of the Researchers Supporting Project (RSP2025R214), King Saud University, Riyadh, Saudi Arabia.

References

1 H. Li, J. Zhang, L. Yang, H. Cao, Z. Yang, P. Yang, W. Zhang, Y. Li, X. Chen and Z. Gu, *Adv. Funct. Mater.*, 2023, **33**, 2212193.
2 J. M. V. Makabenta, A. Nabawy, C.-H. Li, S. Schmidt-Malan, R. Patel and V. M. Rotello, *Nat. Rev. Microbiol.*, 2021, **19**, 23–36.
3 Y. Yu, J. Ding, Y. Zhou, H. Xiao and G. Wu, *Biosaf. Health*, 2022, **4**, 15–22.
4 L. D. Blackman, Y. Qu, P. Cass and K. E. Locock, *Chem. Soc. Rev.*, 2021, **50**, 1587–1616.
5 J. Cheng, G. Gan, S. Zheng, G. Zhang, C. Zhu, S. Liu and J. Hu, *Nat. Commun.*, 2023, **14**, 7510.
6 Y. Yu, F. Bu, H. Zhou, Y. Wang, J. Cui, X. Wang, G. Nie and H. Xiao, *Mater. Chem. Front.*, 2020, **4**, 1930–1953.
7 J. Zhang, H. Guo, M. Liu, K. Tang, S. Li, Q. Fang, H. Du, X. Zhou, X. Lin and Y. Yang, *Exploration*, 2023, 20230087.
8 F. Bu, X. Kang, D. Tang, F. Liu, L. Chen, P. Zhang, W. Feng, Y. Yu, G. Li and H. Xiao, *Bioact. Mater.*, 2024, **33**, 341–354.
9 Y. Shi, Y. Cao, J. Cheng, W. Yu, M. Liu, J. Yin, C. Huang, X. Liang, H. Zhou and H. Liu, *Adv. Funct. Mater.*, 2022, **32**, 2111148.
10 M. Ye, Y. Zhao, Y. Wang, M. Zhao, N. Yodsanit, R. Xie, D. Andes and S. Gong, *Adv. Mater.*, 2021, **33**, 2006772.
11 J. Huo, Q. Jia, H. Huang, J. Zhang, P. Li, X. Dong and W. Huang, *Chem. Soc. Rev.*, 2021, **50**, 8762–8789.
12 Z. Yi, G. Chen, X. Chen, X. Ma, X. Cui, Z. Sun, W. Su and X. Li, *ACS Appl. Mater. Interfaces*, 2020, **12**, 33550–33563.
13 P. Makvandi, C. y. Wang, E. N. Zare, A. Borzacchiello, L. n. Niu and F. R. Tay, *Adv. Funct. Mater.*, 2020, **30**, 1910021.
14 Y. Yu, D. Tang, C. Liu, Q. Zhang, L. Tang, Y. Lu and H. Xiao, *Adv. Mater.*, 2022, **34**, 2105976.
15 J. Ma and C. Wu, *Exploration*, 2022, **2**, 20210083.
16 Y. Yu, R. Tian, Y. Zhao, X. Qin, L. Hu, J. J. Zou, Y. W. Yang and J. Tian, *Adv. Healthcare Mater.*, 2023, **12**, 2201651.
17 X. Zhang, Z. Zhang, Q. Shu, C. Xu, Q. Zheng, Z. Guo, C. Wang, Z. Hao, X. Liu and G. Wang, *Adv. Funct. Mater.*, 2021, **31**, 2008720.
18 Y. Zhao, Z. Zhang, Z. Pan and Y. Liu, *Exploration*, 2021, **1**, 20210089.
19 S. Li, Y. Yang, S. Wang, Y. Gao, Z. Song, L. Chen and Z. Chen, *Exploration*, 2022, **2**, 20210223.
20 G. Fang, W. Li, X. Shen, J. M. Perez-Aguilar, Y. Chong, X. Gao, Z. Chai, C. Chen, C. Ge and R. Zhou, *Nat. Commun.*, 2018, **9**, 129.
21 L. Laloux, D. Kastrati, S. Cambier, A. C. Gutleb and Y. J. Schneider, *Small*, 2020, **16**, 1907687.
22 Y. Chen, L. Ren, L. Sun, X. Bai, G. Zhuang, B. Cao, G. Hu, N. Zheng and S. Liu, *NPG Asia Mater.*, 2020, **12**, 56.
23 Y. Yu, Y. Zhang, Y. Cheng, Y. Wang, Z. Chen, H. Sun, X. Wei, Z. Ma, J. Li and Y. Bai, *Bioact. Mater.*, 2022, **13**, 269–285.
24 S. Cheng, M. Qi, W. Li, W. Sun, M. Li, J. Lin, X. Bai, Y. Sun, B. Dong and L. Wang, *Adv. Healthcare Mater.*, 2023, **12**, 2202652.
25 W. Wang, Y. Gao, W. Xu, Y. Xu, N. Zhou, Y. Li, M. Zhang and B. Z. Tang, *Adv. Mater.*, 2024, **36**, 2307785.
26 H. Zhou, Y. Liao, X. Han, D. S. Chen, X. Hong, K. Zhou, X. Jiang, Y. Xiao and J. Shi, *Nano Lett.*, 2023, **23**, 3661–3668.
27 J. Zheng, H. Liu, S.-H. Chen, B. Huang, T. Tang, P. Huang and R. Cui, *Anal. Chem.*, 2024, **96**, 5315–5322.
28 Z. Geng, Z. Cao and J. Liu, *Exploration*, 2023, **3**, 20210117.
29 B. Yu, Y. Wang, T. Bing, Y. Tang, J. Huang, H. Xiao, C. Liu and Y. Yu, *Adv. Mater.*, 2024, **36**, 2310456.
30 D. Wei, Y. Yu, X. Zhang, Y. Wang, H. Chen, Y. Zhao, F. Wang, G. Rong, W. Wang and X. Kang, *ACS Nano*, 2020, **14**, 16984–16996.

31 G. Xiong, D. Huang, L. Lu, X. Luo, Y. Wang, S. Liu, M. Chen, S. Yu, M. Kappen and C. You, *Small Methods*, 2022, **6**, 2200379.
32 R. Li, Z. Chen, Z. Dai and Y. Yu, *Cancer Biol. Med.*, 2021, **18**, 388.
33 Z. Liu, X. Chen, W. Ling, M. Wang, B. Qiu and J. Shi, *Polym. Compos.*, 2024, **45**, 3448–3459.
34 C. Lochenie, S. Duncan, Y. Zhou, L. Fingerhut, A. Kiang, S. Benson, G. Jiang, X. Liu, B. Mills and M. Vendrell, *Adv. Mater.*, 2024, e2404107, DOI: **10.1002/adma.202404107**.
35 A. Sirelkhatim, S. Mahmud, A. Seeni, N. H. M. Kaus, L. C. Ann, S. K. M. Bakhori, H. Hasan and D. Mohamad, *Nano–Micro Lett.*, 2015, **7**, 219–242.
36 A. F. El-Sayed, W. M. Aboulthana, M. A. Sherief, G. T. El-Bassyouni and S. M. Mousa, *Sci. Rep.*, 2024, **14**, 9027.
37 I. Ullah, S. S. Khan, W. Ahmad, L. Liu, A. Rady, B. Aldahmash, Y. Yu, J. Wang and Y. Wang, *Commun. Chem.*, 2024, **7**, 131.
38 S. S. Khan, I. Ullah, S. Zada, A. Ahmad, W. Ahmad, H. Xu, S. Ullah and L. Liu, *Materials*, 2022, **15**, 4813.
39 V. Harish, M. Ansari, D. Tewari, A. B. Yadav, N. Sharma, S. Bawarig, M.-L. García-Betancourt, A. Karatutlu, M. Bechelany and A. Barhoum, *J. Taiwan Inst. Chem. Eng.*, 2023, **149**, 105010.
40 M. H. A. Elella, A. E. Shalan, M. W. Sabaa and R. R. Mohamed, *RSC Adv.*, 2022, **12**, 1095–1104.
41 V. Shah, D. Medina-Cruz, A. Vernet-Crua, L. B. Truong, E. Sotelo, E. Mostafavi, M. U. González, J. M. García-Martín, J. L. Cholula-Díaz and T. J. Webster, *J. Funct. Biomater.*, 2022, **14**, 24.
42 A. Muthu, D. Sári, A. Ferroudj, H. El-Ramady, Á. Béni, K. Badgar and J. Prokisch, *Appl. Sci.*, 2023, **13**, 11733.
43 L. Kosaristanova, Z. Bytesnikova, T. Fialova, J. Pekarkova, P. Svec, F. Ondreas, V. Jemelikova, A. Ridoskova, P. Makovicky and L. Sivak, *J. Anim. Sci. Biotechnol.*, 2024, **15**, 1–17.
44 P. Gao, S. Feng, Q. Wang, N. Wang, L. Li, J. Sun, X. Shi, B. Zhou and W. Li, *Authorea*, 2023, preprint, DOI: **10.22541/au.168475029.99475478/v1**.
45 M. Jayanetti, C. Thambiliyagodage, H. Liyanaarachchi, G. Ekanayake, A. Mendis and L. Usgodaarachchi, *Sci. Rep.*, 2024, **14**, 1293.
46 Y. Gao, Z. Li, J. Huang, M. Zhao and J. Wu, *J. Mater. Chem. B*, 2020, **8**, 8768–8780.
47 H. Li, Y. Yuan, L. Zhang, C. Xu, H. Xu and Z. Chen, *Adv. Sci.*, 2024, **11**, 2305363.
48 W. Li, W. Duan, G. Liao, F. Gao, Y. Wang, R. Cui, J. Zhao and C. Wang, *Nat. Commun.*, 2024, **15**, 6763.
49 Y. Huang, Z. Du, K. Li, W. Jing, P. Wei, B. Zhao, Y. Yu, Q. Cai and X. Yang, *Adv. Fiber Mater.*, 2022, **4**, 894–907.
50 C. Yuan, D. Zhang, Y. Tang, Z. Guo, K. Lin, Y. Yu, J. Li and Q. Cai, *Biomater. Adv.*, 2023, **149**, 213387.
51 I. Ullah, S. S. Khan, W. Ahmad, L. Liu, A. Rady, B. Aldahmash, C. Yu and Y. Wang, *RSC Adv.*, 2024, **14**, 18871–18878.
52 Y. Gao, L. Wang, C. Zhou, Y. Zhao, H. Huang and J. Wu, *Chin. Chem. Lett.*, 2024, 110028.
53 X. Qian, T. Lu, C. Huang, D. Zheng, G. Gong, X. Chu, X. Wang, H. Lai, L. Ma and L. Jiang, *Adv. Funct. Mater.*, 2024, 2315576.
54 H. Zhou, D. Tang, X. Kang, H. Yuan, Y. Yu, X. Xiong, N. Wu, F. Chen, X. Wang and H. Xiao, *Adv. Sci.*, 2022, **9**, 2200732.
55 X. Bao, S. Huo, Z. Wang, S. Yang, L. Dou, Y. Liu, J. Huang, C. Cai, B. Fang and G. Xu, *J. Nanobiotechnol.*, 2024, **22**, 80.
56 P. Dam, M. Celik, M. Ustun, S. Saha, C. Saha, E. A. Kacar, S. Kugu, E. N. Karagulle, S. Tasoglu and F. Buyukserin, *RSC Adv.*, 2023, **13**, 21345–21364.